



Vertical convection regimes in a two-dimensional rectangular cavity: Prandtl and aspect ratio dependence

Arman Khoubani¹, Ashwin Vishnu Mohanan², Pierre Augier¹ and Jan-Bert Flór^{1,†}

¹Laboratoire des Écoulements Géophysiques et Industriels, Université Grenoble Alpes, CNRS, Grenoble INP, 38000 Grenoble, France

²Swedish Meteorological and Hydrological Institute, SE-601 76 Norrköping, Sweden

(Received 28 April 2023; revised 23 November 2023; accepted 6 December 2023)

Vertical convection is the fluid motion that is induced by the heating and cooling of two opposed vertical boundaries of a rectangular cavity (see e.g. Wang *et al.*, *J. Fluid Mech.*, vol. 917, 2021, A6). We consider the linear stability of the steady two-dimensional flow reached at Rayleigh numbers of $O(10^8)$. As a function of the Prandtl number, Pr , and the height-to-width aspect ratio of the domain, A , the base flow of each case is computed numerically and linear simulations are used to obtain the properties of the leading linear instability mode. Flow regimes depend on the presence of a circulation in the entire cavity, detachment of the thermal layer from the boundary or the corner regions and on the oscillation frequency relative to the natural frequency of oscillation in the stably temperature-stratified interior, allowing for the presence of internal waves or not. Accordingly, the regime is called slow or fast, respectively. Either the global circulation or internal waves in the interior may couple the top and bottom buoyancy currents, while their absence implies asymmetry in their perturbation amplitude. Six flow regimes are found in the range of $0.1 \leq Pr \leq 4$ and $0.5 \leq A \leq 2$. For $Pr \lesssim 0.4$ and $A > 1$, the base flow is driven by a large circulation in the entire cavity. For $Pr \gtrsim 0.7$, the thermal boundary layers are thin and the instability is driven by the motion along the wall and the detached boundary layer. A transition between these regimes is marked by a dramatic change in oscillation frequency at $Pr = 0.55 \pm 0.15$ and $A < 2$.

Key words: convection in cavities, buoyant boundary layers

† Email address for correspondence: jan-bert.flor@univ-grenoble-alpes.fr

1. Introduction

Over the past six decades, vertical convection has attracted significant interest due to its wide range of applications in industry, the environment and geophysics. Circulation patterns and instabilities that may arise due to vertical heat transport along hot or cold isothermal boundaries are relevant in view of the transport of heat (see e.g. Miroshnichenko & Sheremet 2018). In the idealised case of a rectangular cavity, the typical flow evolution is such that, after turning on the heat forcing above its critical value for convection, an upward motion arises at the heated boundary and a downward motion at the cooled boundary, while stratification develops progressively in the interior (Gill 1966). When these motions reach the two horizontal adiabatic boundaries, they turn into horizontal buoyancy currents. The flow patterns in this cavity and related instabilities are determined by the Rayleigh number, the Prandtl number and the aspect ratio defined respectively as

$$Ra = \frac{g\beta\Delta TH^3}{\nu\kappa} \quad Pr = \frac{\nu}{\kappa} \quad \text{and} \quad A = \frac{H}{W}, \quad (1.1a-c)$$

with β the thermal expansion coefficient, ν the dynamic viscosity, κ the thermal diffusivity, H and W the height and width of the cavity, ΔT the horizontal temperature difference in the cavity and g the gravitational constant. In view of the relatively low aspect ratio considered ($A < 4$), the Rayleigh number is based on the height H of the tank, as is most common (see e.g. Bejan 2013), allowing also for comparison with other results in the literature. In this study, we consider the linear instability of the steady circulating flow that is reached at intermediate critical Rayleigh numbers $O(10^8)$ beyond the onset of the convective instability for a range of Prandtl numbers. This steady circulating flow is later called the base flow.

Applications vary with Prandtl number. Generally, higher Prandtl numbers apply to geophysical flows with Prandtl numbers of 0.7 and 7 for air and water at 20 °C, respectively, and very high Prandtl numbers for the Earth's mantle, with magma viscosities somewhere around 10^{19} (e.g. Busse 2006). For seawater the Prandtl number is in the range $1 < Pr < 14$ as a function of temperature and salinity. The lower Prandtl numbers apply to gases and liquid metals. Atmospheric air has a Prandtl number in the range of $0.7 < Pr < 0.79$, methane gas in the range of $0.7 < Pr < 0.87$, whereas a mixture of liquid helium may have a Prandtl number in the range $0.2 < Pr < 0.6$ depending on its mixture. Other applications are semiconductor crystals with $Pr O(10^{-2})$ (see e.g. Gelfgat, Bar-Yospeh & Yarin 1999), and nuclear engineering processes that are associated with convective fluid motions of sodium, lead or alloys for cooling with $Pr \approx 10^{-1}$ to 10^{-3} (see e.g. Grötzbach 2013). Very small Prandtl numbers apply to astrophysics, stellar and deep solar convection with $Pr \approx 10^{-6}$ (see e.g. Guervilly, Cardin & Schaeffer 2019; Garaud 2021; Pandey, Schumacher & Sreenivasan 2021, etc.).

In the past, particular attention has been given to the flow transition to a permanent oscillatory state that occurs in the corner regions of a cavity with $A = 1$ for $Pr = 0.7$ and a Rayleigh number just above critical, i.e. $Ra \approx 10^8$. The thermal boundary layers detach and the presence of standing and dissipative internal wave modes were observed in the interior (see Paolucci & Chenoweth 1989; Henkes & Hoogendoorn 1990; Le Quéré & Behnia 1998, and references therein). Above the critical Rayleigh number, a shear instability occurs in the vertical boundary layers, with a transition to chaos through quasi-periodicity (see e.g. Lappa 2009). For larger Prandtl numbers, differences in behaviour occur since the thermal boundary layer is thinner with a larger velocity gradient normal to the boundary, favouring shear instability. Thus, an immediate transition to turbulence has been observed for Prandtl

numbers, $2.5 \leq Pr \leq 7.0$, and a transition from steady to a periodic state of the jet-like structure for the lower Prandtl number range $0.25 \leq Pr \leq 2.0$ (see Chenoweth & Paolucci 1986; Janssen & Henkes 1995).

For tall cavities with $1.0 \leq A \leq 3.0$ ($Pr = 0.7$) (see e.g. Xin & Le Quéré 2006, and references therein), the instability is determined by the detachment of the boundary layer in the corner regions and the spatial structure of normal modes that fill the cavity. The instability in the boundary remains relatively small. The inclined flow structures in the interior that were ascribed to internal waves (see Le Quéré & Behnia 1998; Xin & Le Quéré 1995) are shown to be in fact part of the unstable mode (Xin & Le Quéré 2006). For cavities with $A \geq 3$, the travelling waves in the vertical boundaries have approximately 10 times higher frequencies with the instability in the vertical boundary layers being dominant. These wall mode waves occur as Tollmien–Schlichting waves in the boundary layer for small Ra (Yahata 1999; Xin & Le Quéré 2006; Xin & Le Quéré 2012). For smaller values of A , internal waves in the interior dominate the instability (Yahata 1999). The instability mode is found to be either centrosymmetric or anti-centrosymmetric, respectively. This instability is part of two Hopf bifurcations that are encountered for increasing Ra (and fixed Pr), with consecutively the (anti-centrosymmetric or centrosymmetric) internal wave modes, and for larger Rayleigh number the (anti-centrosymmetric or centrosymmetric) wall modes (see Burroughs *et al.* 2004; Oteski *et al.* 2015).

For larger Ra , the flow becomes nonlinear with vortices detaching from the boundary layer and penetrating into the stratified core. These penetrating vortices excite internal waves with a frequency smaller than the Brunt–Väisälä frequency, thus perturbing the core fluid (Xin & Le Quéré 1995). The instability in a rectangular cavity can thus form in the corner region or in the lateral boundary, and internal waves take part in the instability. Next to the instability, for certain parameters, a large-scale circulation has also been observed with the hot boundary layer motion ‘connecting’ to the start of the cold boundary layer motion. In the case of conducting horizontal boundaries, this gives rise to limit cycles (see Henkes & Hoogendoorn 1990). A comprehensive review of studies on vertical convection is given in a historical perspective by Le Quéré (2022).

Although a range of Prandtl numbers and different aspect ratios have been considered in the past, the critical Rayleigh number and the shape and symmetry of the most unstable corresponding mode are known only for some specific values of Pr and A . There are no clear indications as to the mechanism responsible for the instability, the presence of locally increasing modes or global modes and their symmetry. In this research, in order to obtain information about the shape of the most unstable mode and the critical Rayleigh number, a numerical linear stability analysis is used. The representation of the perturbations of amplitude, phase and vorticity of each specific unstable mode allows investigation of the mechanism of instability and the role of internal waves, permitting different flow regimes to be identified.

Apart from the reduced computational costs, the advantage of a two-dimensional approach is that it is well posed with a simple geometry and forcing, similar to other flows for which the knowledge and understanding of regimes and the transition between them is of fundamental interest. Some well known other examples are Taylor–Couette flow or Rayleigh–Bénard flow in thin gaps. More related flows are the shear-driven cavity flow (see e.g. for the homogeneous case Bengana *et al.* (2019), and for the stratified case Wu, Welfert & Lopez 2018), or the self-organised state of two-dimensional turbulence on a rectangular domain interacting with vorticity generated at the slip-free boundaries (van de Konijnenberg, Flor & van Heijst 1998; van Heijst, Clercx & Molenaar 2006). In the latter example, a large central vortex interacts with the boundaries, implying aspects of

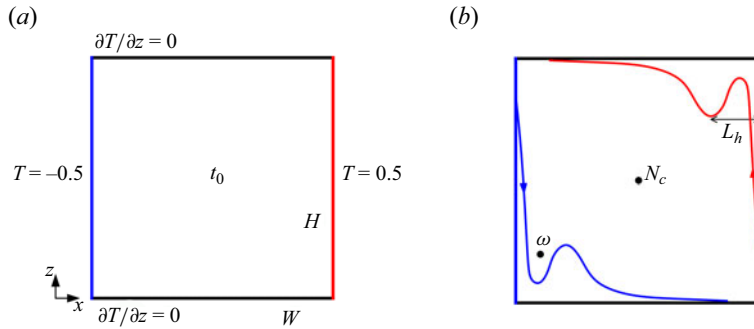


Figure 1. (a) Schematic of the problem with the walls kept at constant temperatures 0.5 and -0.5 so that $\Delta T = 1.0$. The initial condition for the nonlinear simulations is $T_0 = \Delta T \times (x/x_{max} - 0.5) + \text{noise}$ and $(u, v) = (0, 0)$, and for the linear simulations, $T_{p0} = \text{noise}$ and $(u_p, v_p) = (0, 0)$. (b) Location of the interrogation points used to assess the state of the flow with the oscillation frequency ω measured in the corner at $(x, z) = (0.1, 0.1)$, for $A = 1$, $H = (0, 1)$ and $W = (1, 0)$, N_c being the stratification in the centre of the cavity. The maximum speed in the buoyancy current is sketched by red and blue curved lines. Here, L_h is the horizontal distance from the wall to the minimum (in z) on the red line of the current at the top.

symmetry with flow phenomena analogous to large cell flows in vertical convection, but without baroclinic effects.

In a three-dimensional box with periodicity in the third direction (see Xin & Le Quéré 2012, for $Pr = 0.7$), the instability starts for a 10 times smaller Rayleigh number. The three-dimensional effects are, however, modest, with low frequency modes losing their stability earlier than in the two-dimensional case. Two-dimensional simulations are found to be also satisfactory for larger aspect ratio ($A = 4$) and capture the general features of buoyancy-driven flow, as long as it is not turbulent, i.e. up to $Ra \sim 10^{10}$ (Trias *et al.* 2007). Also partial similarities to the two-dimensional counterpart have been noticed in cubic cavities (see Gelfgat 2017, 2020a,b). This is further discussed at the end of the conclusions.

In the next section, § 2, the numerical code with the linear approach and the decomposition into leading modes are discussed next to the nonlinear approach and the diagnostics. In the subsequent section, § 3, the results are presented with the different base states, leading linear modes and the different observed regimes. In § 4, the main conclusions are presented and further discussed.

2. Numerical set-up

2.1. Governing equations and linear stability approach

We consider a two-dimensional flow inside a rectangular cavity of aspect ratio $A_v = H/W$ with cavity height H and width W , adiabatic top and bottom boundaries and the two walls kept at a constant temperature with temperature difference ΔT (see figure 1a). The scales of this problem are ΔT for the temperature difference and for the length scales $(x, y) \sim (\delta_T, H)$, where $\delta_T = (\kappa t_r)^{1/2}$ is the thickness of the heated boundary layer, and t_r is the reference time defined below. Using the momentum equations, the friction term then scales with the buoyancy term, i.e. $\nu V_r / (\delta_T)^2 \sim g\beta\Delta T$, which yields a characteristic speed $V_r = (\kappa/H)Ra^{1/2}$. The time scale $t_r = H/V_r$ is obtained from the balance between the advective term and diffusive term in the temperature equation. With these scales, one obtains for the dimensionless form of the continuity equation, Boussinesq approximation

Nonlinear temperature signal

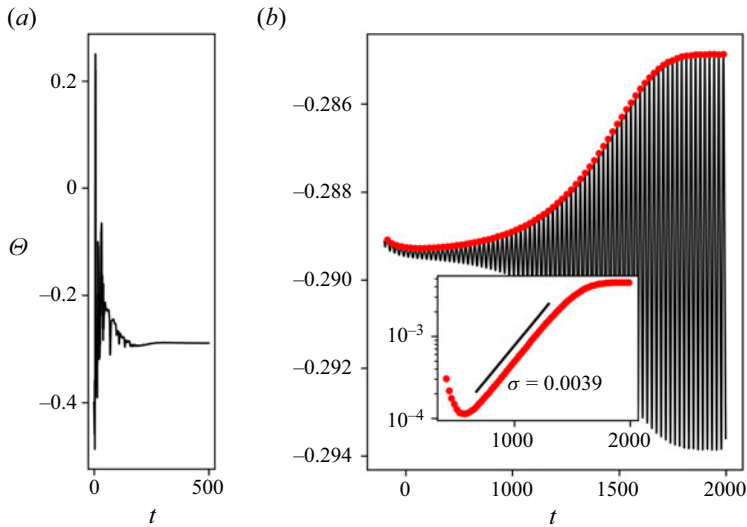


Figure 2. Temperature signal of a nonlinear simulation at point $(x, z) = (0.1, 0.1)$ for $A = 1.0$, $Pr = 0.71$ and $Ra = 1.85 \times 10^8$, with (a) the evolution of the flow from $t = 0$, and (b) the evolution to a steady state and subsequent exponential growth in amplitude and saturation. The inset shows the perturbation in log scale with the fit giving the growth rate (straight line).

of the Navier–Stokes equations and the temperature equations, respectively,

$$\nabla \cdot \mathbf{v} = 0, \tag{2.1}$$

$$\frac{\partial \mathbf{v}}{\partial t} + \mathbf{v} \cdot \nabla \mathbf{v} = -\nabla P + \frac{Pr}{Ra^{1/2}} \nabla^2 \mathbf{v} + Pr \Theta \mathbf{e}_z, \tag{2.2}$$

$$\frac{\partial \Theta}{\partial t} + \mathbf{v} \cdot \nabla \Theta = \frac{1}{Ra^{1/2}} \nabla^2 \Theta, \tag{2.3}$$

with \mathbf{v} the velocity vector, pressure P and Θ the dimensionless temperature $(T - T_r)/\Delta T$, with T_r being the average temperature (here, $T_r = 0$). As mentioned above, the control parameters of this flow are the Rayleigh number, Prandtl number and aspect ratio $A = H/W$, which depends on the chosen length W since the height H is kept constant.

The no-slip condition is used for all boundaries. For the temperature, the Dirichlet condition is used with $\Theta = 0.5$ and $\Theta = -0.5$ on the two lateral walls, and for zero heat flux the Neumann condition at the two horizontal boundaries.

Numerical simulations are performed with the spectral element code Nek5000 (<https://nek5000.mcs.anl.gov>) using the two newly developed Python packages Snek5000 (<https://snek5000.readthedocs.io>) and Snek5000-cbox (<https://github.com/snek5000/snek5000-cbox>) (Augier, Mohanan & Bonamy 2019; Mohanan *et al.* 2019; Mohanan, Khoubani & Augier 2023). The packages are available online and the data that we have produced here are available as a Zenodo dataset (<https://zenodo.org/record/7827872>).

Tests have been conducted for $Pr = 0.71$ and $A = 1$ and results for the growth rate and oscillation frequency have been validated with respect to former studies in the literature. The resolution employed (see table 1 in the Appendix) allows for the study of the motion in the thin boundary layers near the walls, and accuracy in growth rate and oscillation frequency. Figure 2 shows a typical temperature signal measured in the corner of the cavity (see figure 1b) for the nonlinear simulation. The large difference in temperature between

figures 2(a) and 2(b) reveals the transient to the base state ($t < 250$) and the subsequent growth and saturation of the instability ($t > 250$), respectively. From $t = 0$ to 250, the motions along the boundaries and the stratification in the interior develop. The base state is a steady state with minimum amplitude of oscillations (at approximately $t \approx 500$), with motions in thermal boundary layers in the presence of a stratified interior. From $t = 500$ onwards, a linear instability leads to the exponential growth of the amplitude of the oscillation up until approximately $t = 1375$, after which it saturates and small nonlinear oscillations in amplitude develop. The oscillation frequency shows a perfect exponential growth in the range of approximately $500 < t < 1400$ (see the inset in figure 2b).

For each set of control parameters Pr and A , nonlinear simulations are performed to obtain a first approximation of the critical Rayleigh number Ra_c . Nonlinear simulations reach a steady state at a Rayleigh number of $O(\sim 10^8)$ but still smaller than the critical Rayleigh number, i.e. $Ra < Ra_c$, while for slightly higher Ra values, the flow starts to oscillate at $t \approx 500$. Three nonlinear simulations are performed for three values of Ra slightly larger than the estimated Ra_c using the selective frequency damping (SFD) method of Åkervik *et al.* (2006), which give us three steady base states. This method has also been used recently for computing the base state of the flow that is induced when tilting a cavity containing a stably stratified fluid (see Grayer *et al.* 2020).

Subsequently, the linear stability of these steady base flows is considered. Using perturbed variables $\Theta = \Theta_b + \theta'$, $\mathbf{V} = \mathbf{V}_b + \mathbf{v}'$, $P = P_b + p'$ where subscript b represents the base state and superscript $'$ the perturbation, and neglecting second-order terms, we obtain linearised perturbation equations of the form

$$\frac{\partial \mathbf{v}'}{\partial t} + \mathbf{V}_b \cdot \nabla \mathbf{v}' + \mathbf{v}' \cdot \nabla \mathbf{V}_b = -\nabla p' + \frac{Pr}{Ra^{1/2}} \nabla^2 \mathbf{v}' + Pr \theta' \mathbf{e}_z, \quad (2.4)$$

$$\frac{\partial \theta'}{\partial t} + \mathbf{V}_b \cdot \nabla \theta' + \mathbf{v}' \cdot \nabla \Theta_b = \frac{1}{Ra^{1/2}} \nabla^2 \theta'. \quad (2.5)$$

Linear simulations are run for the three steady base states obtained from the SFD method, and corresponding to three unstable Ra values. A small amount of noise of the order of 10^{-6} is added so that, due to the linear instability, an exponential growth of the leading mode is observed in the whole cavity. This noise is random and therefore not necessarily symmetric. Then, the growth rate is determined for each linear simulation, thus providing eventually three different growth rates. Using a linear interpolation of these growth rates, the critical Rayleigh number Ra_c is extrapolated from the value for zero growth rate. The base flow and the perturbation analysed in the next section are obtained from the nonlinear and linear simulations for the Rayleigh number just above this critical Rayleigh number.

2.2. Decomposition of the leading linear mode

In view of former observations of this instability (see e.g. Xin & Le Quéré 2006), the different variables can be decomposed during the oscillating exponential growth into

$$\theta'(x, z, t) = A_\theta(x, z) \cos(\omega t + \Phi_\theta(x, z)) e^{\sigma_r t}, \quad (2.6)$$

$$u'(x, z, t) = A_u(x, z) \cos(\omega t + \Phi_u(x, z)) e^{\sigma_r t}, \quad (2.7)$$

and

$$w'(x, z, t) = A_w(x, z) \cos(\omega t + \Phi_w(x, z)) e^{\sigma_r t}, \quad (2.8)$$

where $A(x, z)$, ω , $\Phi(x, z)$ and σ_r are amplitude, frequency, phase and growth rate of the field variables, respectively. The growth rate σ and the oscillation frequency ω are

Vertical convection regimes

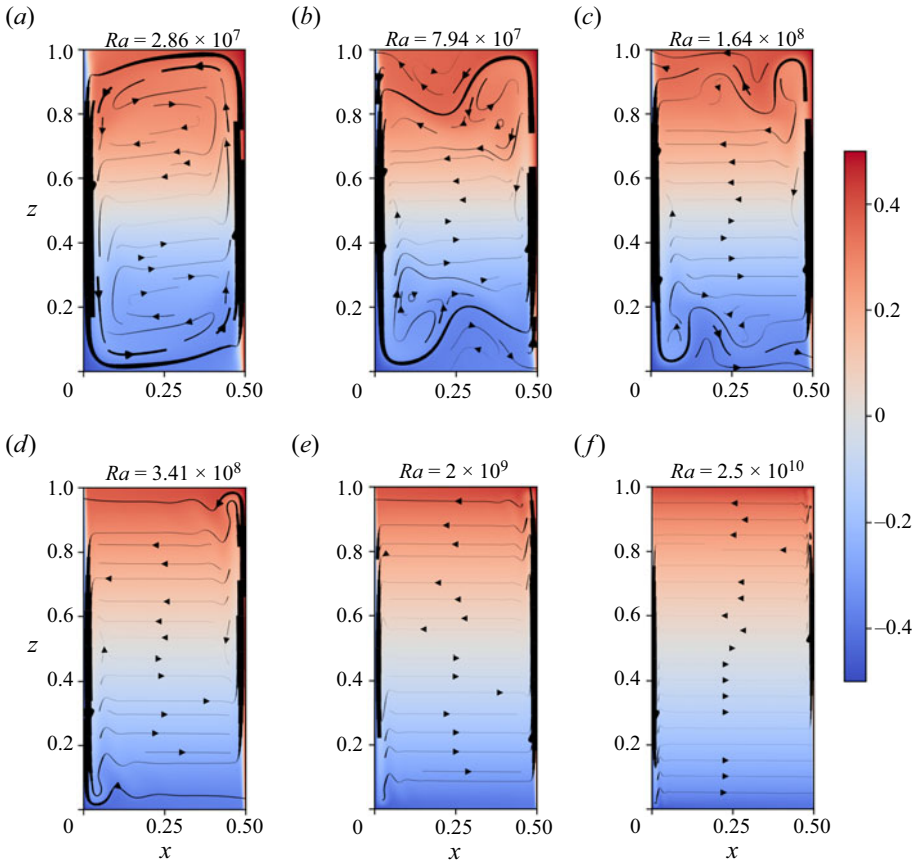


Figure 3. The base flow states for $A = 2.0$ and different Pr : (a) $Pr = 0.35$, (b) $Pr = 0.53$, (c) $Pr = 0.71$, (d) $Pr = 1.4$, (e) $Pr = 2.0$ and (f) $Pr = 2.8$. Streamlines are supplied with arrows indicating flow direction, and colour representing the temperature.

computed by an algorithm based on Hilbert transforms. The amplitude fields are then obtained by taking the time maximum of the perturbation variables divided by $e^{\sigma t}$. Finally, the phase fields are obtained with one curve fit per grid point and variable.

3. Numerical results

3.1. The steady base flow and diagnostics

Figure 3(a–f) shows the steady base flow for different Prandtl numbers and constant aspect ratio $A = 2.0$. From figure 3(a–f) one notices that, for larger Prandtl numbers, the buoyancy currents detach and meander along the horizontal boundaries, the number of meanders depending on the Pr . Clear experimental and numerical support for this meandering is shown by Xu, Patterson & Lei (2008). The wavelength of this meandering buoyancy current changes significantly with Pr , while its presence is limited by the horizontal extent W of the cavity represented by A (note H is kept constant). When the width of the cavity is smaller than this wavelength, the head of the buoyancy current joins the start of the cold boundary layer, and *vice versa* near the bottom boundary, such that the two currents reinforce each other's inertia, leading to a large-scale fast circulation

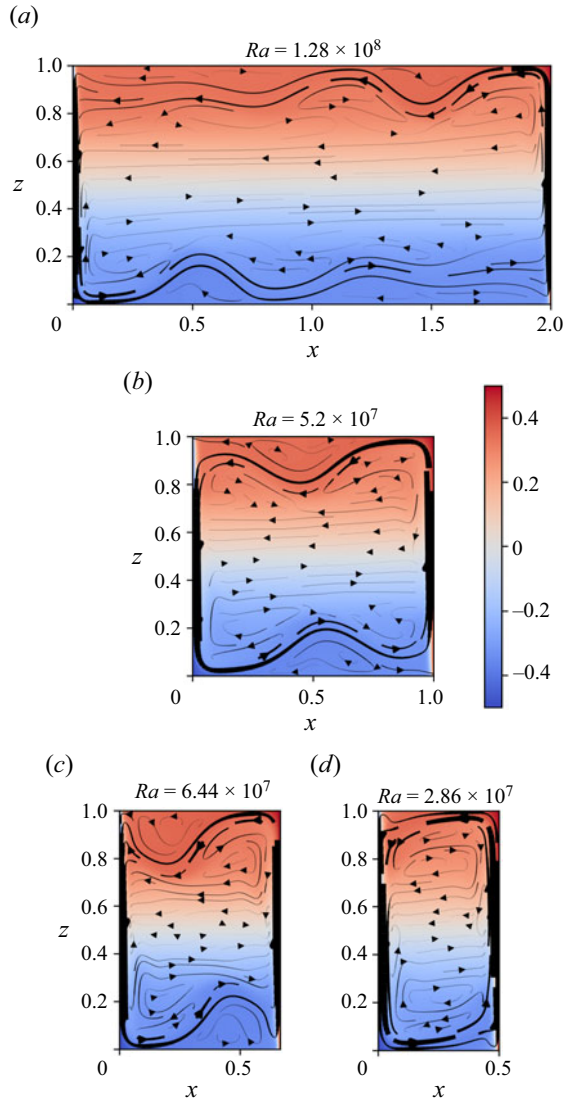


Figure 4. The base flow state for $Pr = 0.35$ and different A : (a) $A = 0.5$, (b) $A = 1.0$, (c) $A = 1.5$ and (d) $A = 2.0$. Lines show the streamlines with the arrows giving the flow direction, and colour representing the temperature.

along the boundaries (see figure 3a). With increasing Pr ($Pr < 0.7$ in figure 3), the large-scale circulation decreases in strength and the buoyancy current detaches from the horizontal boundary, i.e. $L_h < W$, and it meanders locally. For larger Pr values, ($Pr > 1$, see figure 3d–f) a horizontal exchange flow establishes in the interior between the two thermal boundary layers. The boundary layers are thinner for these higher Pr values. For a constant Pr it depends on the aspect ratio whether there are cell patterns (as in figure 3a) or rather horizontal exchanges between the thermal boundary layers (as in figure 3f) (see Xin & Le Quéré 2006).

Figure 4 shows flows for $Pr = 0.35$ and varying aspect ratio A . When the width of the cavity is large (see figure 4a for $A = 0.5$), the buoyancy current meanders along the horizontal boundary. With increasing aspect ratio A , the meander length scale of the

buoyancy current becomes smaller than the width of the cavity, and there is an increasing tendency for the formation of cell circulation. Two circulation cells appear for $A = 2$ in [figure 4\(d\)](#).

In all cases, a stable density gradient $-\beta dT/dz$ is present in the interior. The buoyancy (Brunt–Väisälä) frequency scaled with time $t_r = H^2/(\kappa Ra^{1/2})$ is given by

$$(N_c t_r)^2 = g\beta \frac{dT}{dz} \frac{H^4}{\kappa^2} \frac{1}{Ra} = Pr \frac{H}{\Delta T} \frac{dT}{dz}, \quad (3.1)$$

showing that the Prandtl number, height of the reservoir and density gradient are relevant for the scaled buoyancy frequency, with slightly stronger stratifications for shallow cavities (small A) and weaker stratifications for high and narrow cavities (large A).

In the simulations, the buoyancy frequency N_c is determined by the density gradient in a small region around the centre of the tank. The meander length scale of the buoyancy current, L_h , is defined as the horizontal distance from the wall where the line that describes the maximum speed (see [figure 1b](#)) has a minimum in z . Here, L_h has been determined from the flow near the top. In the perturbed state, the instability causes oscillations in the temperature with frequency, ω . Its amplitude increases due to the linear instability, and although present in the entire tank, the oscillations are mainly visible in the corner regions where the thermal motion along the wall is blocked by the horizontal boundary (see e.g. [Le Quéré & Behnia 1998](#); [Xin & Le Quéré 2006](#), and references therein). Thus, to analyse this flow, the frequency of the oscillation frequency of the instability mode, ω , the density stratification in the interior, N_c and the wavelength of the meandering buoyancy current, L_h , are measured at the locations shown in [figure 1\(b\)](#).

When the temperature oscillations have a higher frequency than the buoyancy frequency, i.e. $\omega > N_c$, internal waves cannot propagate in the interior and are evanescent. In contrast, when $\omega < N_c$, the buoyancy currents near top and bottom boundaries may couple due to the internal waves that propagate into the interior. Even though a larger value of N may exist near the top and bottom boundaries, the value N_c in the centre of the tank is taken as reference value since it is more relevant for the coupling of the top and bottom regions. As mentioned, flows with $\omega/N_c > 1$ are called fast, and flows with $\omega/N_c < 1$ slow since they allow for the propagation of internal gravity waves, and, in most cases, for the coupling between the two buoyancy currents. In the absence of internal waves, top and bottom instabilities generally start to grow independently with different perturbation amplitudes, resulting in asymmetry. This is referred to as amplitude asymmetry, or asymmetry in short, and is further detailed below.

For the base states, [figure 5\(a\)](#) shows the (scaled) wavelength of the meandering buoyancy current L_h/H against Pr for different aspect ratios of the cavity. For small Pr there is no detachment and L_h is larger than the width of the cavity, i.e. $L_h = 1/A$. In this case, the horizontal buoyancy currents and boundary layers at the sidewalls reinforce each other, leading to a large cell circulation. For larger Pr values, the boundary layers are thin and the aspect ratio A has no influence on the value of L_h/H . The effects obtained for decreasing Pr can also be obtained for larger aspect ratio. Boundary layers grow with distance and become thicker and have more inertia, leading to relatively larger values of L_h .

[Figure 5\(b\)](#) shows that the stratification in the interior increases less for $Pr > 0.4$ than for $Pr < 0.4$ since larger gradients form near the horizontal boundaries, and a weaker stratification forms in the interior. The aspect ratio A has an influence on the internal stratification only for smaller Prandtl numbers for which the large cell circulation dominates.

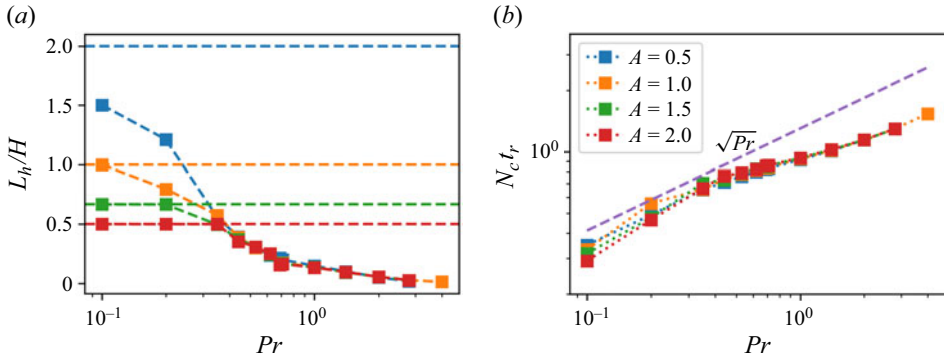


Figure 5. (a) Meander length scale L_h/H against Prandtl number, Pr , with the dashed lines representing the aspect ratios $A = H/W$, and (b) N_c , the Brunt–Väisälä frequency, scaled with the characteristic time t_r at the centre of the cavity as a function of Pr . For comparison, the slope of \sqrt{Pr} predicted by (3.1) is shown by the dashed line.

The asymmetry in the value of the amplitude between the top and bottom currents is considered in particular since its relation to the presence of internal waves is novel and provides new insights. For both currents the growth rates are the same, but due to an asymmetry in the initial noise, the amplitudes of the perturbations may be different. Writing out the equations for the temperature, we have then

$$\theta'(\mathbf{x}, t) = (C_+A_+(\mathbf{x}) + C_-A_-(\mathbf{x})) \cos(\omega t + \phi(\mathbf{x})) e^{\sigma t}, \quad (3.2)$$

with the ratio C_+/C_- depending on the initial noise. Thus, in contrast to the coupled case, with top and bottom currents having the same amplitude and internal waves being part of the same global mode, we have in the uncoupled case two local regions that are growing independently.

The symmetry conditions are imposed by the boundary conditions, so that for a solution Φ with

$$\Phi(\mathbf{x}) = \begin{pmatrix} \Theta_b(\mathbf{x}) \\ V_b(\mathbf{x}) \\ P_b(\mathbf{x}) \\ \xi_b(\mathbf{x}), \end{pmatrix} \quad (3.3)$$

with $\xi_b = \nabla \times V_b$ the vorticity in the basic state, the equations are invariant for the transformations

$$R\Phi(\mathbf{x}) = \begin{pmatrix} -\Theta_b(-\mathbf{x}) \\ -V_b(-\mathbf{x}) \\ P_b(-\mathbf{x}) \\ \xi_b(-\mathbf{x}). \end{pmatrix} \quad (3.4)$$

In case there is symmetry, the solution can be either ‘centro-symmetric’, i.e. $R\Phi(\mathbf{x}) = \Phi(\mathbf{x})$, or ‘anti-centro-symmetric’, i.e. $R\Phi(\mathbf{x}) = -\Phi(\mathbf{x})$ (see Burroughs *et al.* 2004). Counter-intuitively, for centro-symmetry, the velocity phase must be opposite to that in the other corner whereas the vorticity must be equal, and *vice versa* for anti-centro-symmetry. This centro-symmetry was tested considering the point reflected value with respect to the centre of the tank. Thus, the non-dimensional temperature in the top half of the cavity θ'_{top} is compared with its flipped counterpart in the bottom half of the cavity θ'_{bot}^{flip} .

Vertical convection regimes

The parameters for centro-symmetry and anti-centro-symmetry then become, respectively,

$$I_C = \frac{\left\langle \left| \theta'_{top} - \theta'_{bot} \right| \right\rangle}{\sqrt{\langle \theta'^2 \rangle}}, \quad (3.5)$$

$$I_A = \frac{\left\langle \left| \theta'_{top} + \theta'_{bot} \right| \right\rangle}{\sqrt{\langle \theta'^2 \rangle}}, \quad (3.6)$$

with the brackets standing for the average over the domain, and the enumerator representing the root-mean-square value of θ' . When the perturbation is centro-symmetric or anti-centro-symmetric, either I_C or I_A , respectively, is small and never zero because of numerical noise. Both values are large when there is no such symmetry. To identify centro-symmetry, the difference of the reciprocals of I_C and I_A

$$I_{dif} = \frac{1}{I_C} - \frac{1}{I_A}, \quad (3.7)$$

is used, with anti-centro-symmetry for $I_{dif} > 0$, i.e. the temperature perturbations in the top and bottom halves of the cavity have the same sign, and centro-symmetry for $I_{dif} < 0$, i.e. opposite temperature perturbations in the top and bottom halves of the cavity. When $I_{dif} \simeq 0$, there is no symmetry, i.e. the top and bottom currents are asymmetric in amplitude. The expression (3.7) therefore provides simultaneously information about centro-symmetry and amplitude symmetry.

Centro-symmetry is generally better solved with different methods that provide a continuous distribution for the critical Rayleigh number and the centro-symmetry as a function of Prandtl number (see e.g. Lyubimova *et al.* 2009, and references therein). Since this was not the aim of the present investigation, the centro-symmetry below is provided for completeness, and the details are left for future study.

Below, the six observed regimes for increasing Pr are discussed for a single aspect ratio $A = 1$. For the regimes shown in figure 6 the field of the base flow is shown next to the fields of the perturbations predicted by the linear mode decomposition, with (b) amplitude, (c) phase and (d) vorticity. The perturbation of the vorticity field (d) reveals the spatio-temporal nature of the disturbing wave packets. The phase map (c) shows the distribution of the length scales in the field and can be considered as a signature of the internal waves. In addition, two time steps show the base flow perturbed with the linear perturbation (see figure 7a,b).

Movies of the unsteady states are provided as supplementary material available at <https://doi.org/10.1017/jfm.2023.1056>. The effects of varying aspect ratio A , along with the measured parameters ω/N_c and the regime diagram in the space set by A and Pr , are discussed below.

3.2. Six unsteady regimes

The identification of the different regimes, shown in figure 6, is based on the detachment of the buoyancy current from the top and bottom boundaries and/or the location of the instability, the existence of a large-scale circulation and whether the scaled oscillation frequency is slow ($\omega/N_c \leq 1$) or fast ($\omega/N_c > 1$), allowing for the presence of internal waves (or not). With increasing Prandtl number, the plumes detach earlier from the horizontal boundaries, and the presence of internal wave motions in the interior changes

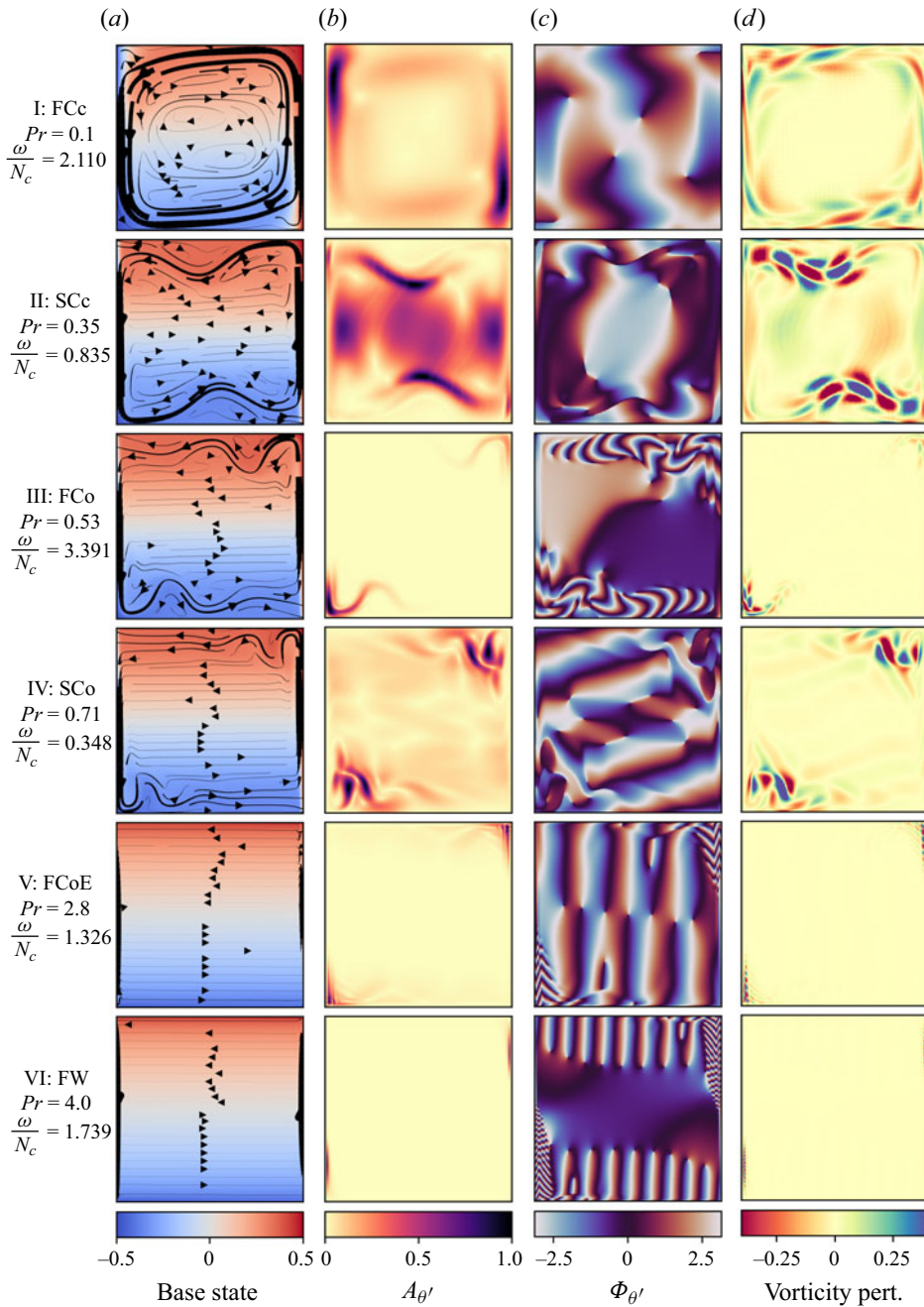


Figure 6. Flow maps for $A = 1.0$ and different different values of Prandtl number, Pr , and oscillation frequency, ω/N_c (cases I–VI), with (a) base state, (b) temperature amplitude $A_{\theta'}$, (c) phase map $\Phi_{\theta'}$ and (d) vorticity perturbation ξ' . Supplementary movies of the regimes I, fast circulation cells (FCc) (movie 1); II, slow circulation cells (SCc) (movie 2); III, fast corner flow (FCo) (movie 3); IV, slow corner flow (SCo) (movie 4); V, fast corner with evanescent waves (FCoE) (movie 5); and VI, fast instabilities at the wall (FW) (movie 6) are available online.

Vertical convection regimes

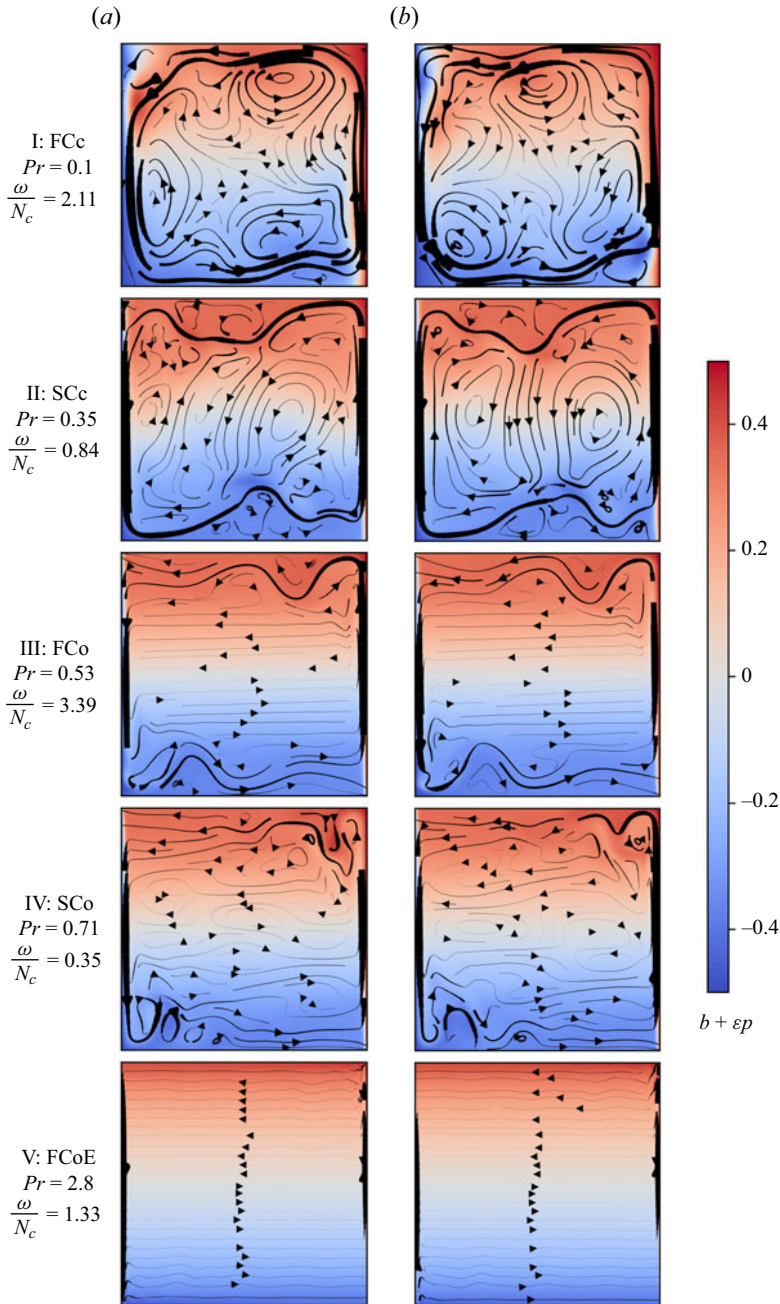


Figure 7. The base flows corresponding to regimes shown in figure 6 plus the perturbation at (a) $t = 0$ and (b) $t = 0.25T$. Arrows on streamlines indicate flow direction and colour represents temperature. Case VI is not shown since differences from case V are very small. For all cases I–VI, the same movies as referred to in figure 6 are represented online.

accordingly (see figure 6 I–VI); figure 7 I–V shows the transition from a convective regime with circulation cells moving locally through the tank to flows confined to boundary currents with horizontal exchange between them. Below we present each flow regime.

In case I ($Pr = 0.1$) (see [figure 6](#)), there is no detachment of the buoyancy current from the horizontal boundaries and the hot buoyancy current joins the cold thermal boundary layer, resulting in a large cell circulation (see e.g. Xin & Le Quéré 2006), thus coupling the top and bottom motions. The phase plot ([figure 6c I](#)) shows a central rotary motion. In the perturbed flow (see [figure 7a,b I](#)) smaller cells move in the interior with the large cell circulation, showing that convective motions dominate. The oscillation frequency of this mode is larger than the buoyancy frequency, $\omega/N_c = 2.26$, and internal waves can therefore not propagate. This flow regime is referred to as the fast cell circulation (FCc).

In case II ($Pr = 0.35$) (see [figure 6 II](#)), the buoyancy current detaches from the boundary and meanders with a wavelength of approximately half the cavity width ([figure 6a II](#)). (Note that for the case $Pr = 0.1$ shown above, an increase in width of the cavity would also result in a detachment of the buoyancy current.) This detachment causes the radiation of internal waves into the interior (see phase plots in [figure 6c II](#)) that have a dominant vertical mode with ω/N_c close to 1.0, leading to quasi vertical iso-phase lines. Vorticity perturbations ([figure 6d II](#)) show a maximum shear in the detached buoyancy current. The perturbed flow ([figure 7a,b II](#)) consists of two large cell structures with a dominant vertical transport, and large oscillations in the density profile, revealing the presence of internal waves. In contrast to the FCc case above, energy of the detached buoyancy currents is dispersed into internal wave motions such that the oscillation frequency is relatively small or ‘slow’. This regime is referred to as slow circulation cells (SCc).

In case III $Pr = 0.53$ (see [figure 6 III](#)) the flow pattern changes from a convective flow to a horizontal exchange flow with a shift in direction at mid-height ([figure 6a III](#)). The buoyancy currents detach from the horizontal boundary close to the thermal wall. Oscillations are fast, $\omega/N_c > 3$, and internal waves cannot propagate through the stratified interior, and the phase plot ([figure 6c III](#)) shows very different length scales in the buoyancy currents compared with those in the interior. In the absence of internal waves and a large-scale circulation, the top and bottom motions are decoupled. Thus, the independent growth of the unstable regions leads to different perturbation amplitudes, implying amplitude asymmetry (see [figure 6b III](#)). Because of the fast oscillations and the localisation of the instability in the corner regions, this flow is referred to as the fast corner flow (FCo).

In case IV $Pr = 0.71$ (see [figure 6 IV](#)), we recover the case studied in detail in former studies (see e.g. Paolucci 1990; Le Quéré & Behnia 1998; Xin & Le Quéré 2006, and references therein), and more recently by Grayer *et al.* (2020). Here, $\omega/N_c \approx 0.5$, allowing for internal waves in the interior. These internal waves and the unstable corner regions are part of the same global instability mode (Xin & Le Quéré 2006) as the phase plot in [figure 6\(c IV\)](#) clearly shows. The amplitude of the internal waves in the interior is relatively weak compared with the amplitude in the corner regions. The perturbed base flow ([figure 7a,b IV](#)) shows next to the oscillating corner regions, recirculating regions in the interior that are slightly flattened by the internal buoyancy stratification. The absolute values of the perturbation amplitude of the top and bottom currents are identical or very close, which is referred to as symmetric in amplitude (not to be confused with centro-symmetry). The vorticity perturbations ([figure 6d IV](#)) have opposite signs at the top and bottom corners, revealing that this mode is anti-centro-symmetric (see the definition in § 3.1), which is the mode that appears for the lowest Rayleigh number, in agreement with Burroughs *et al.* (2004) and Oteski *et al.* (2015). The centro-symmetric mode appears for a slightly higher Rayleigh number.

In case V, $Pr = 2.8$, the thermal boundary layer thickness is thin and the perturbation maxima are limited to very small corner regions ([figure 6a–d V](#)). The oscillation frequency

Vertical convection regimes

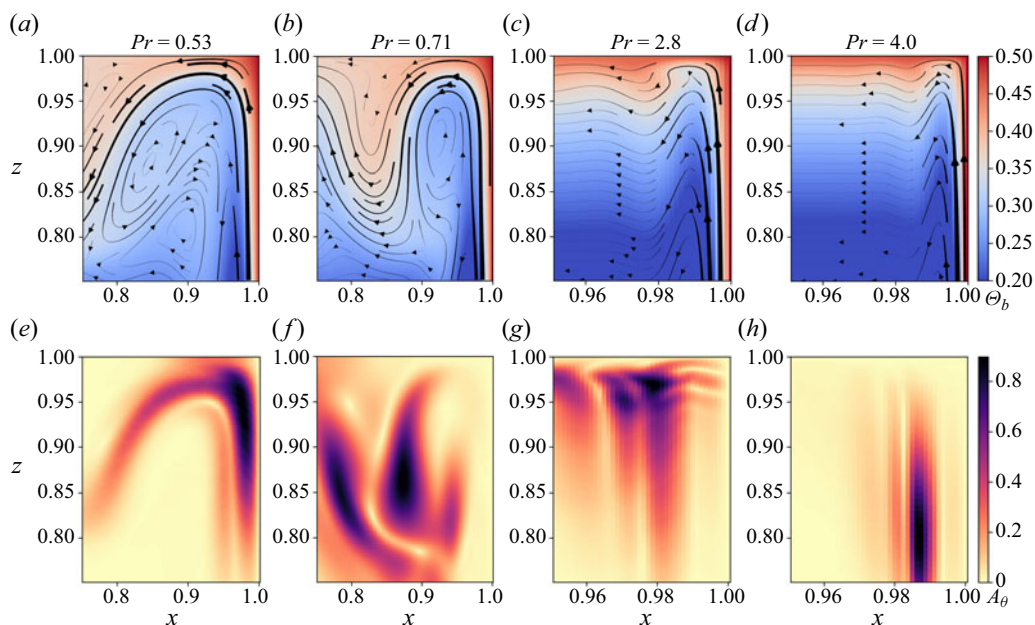


Figure 8. Base flows showing close ups of the streamline–temperature fields of the corner regions for $A = 1$ with maximum amplitude ($a-d$) for Prandtl numbers from 0.53 to 4.0, and ($e-h$) the corresponding amplitude fields. Note that zooms and aspect ratios in ($a,b; e,f$) and ($c,d; g,h$) are chosen differently for visualisation purposes.

is again increased (figure 6c V). Heat is diffused relatively slowly for this Pr so that the temperature gradients near the top and bottom boundaries are larger than in the interior. The scaled oscillation frequency near the boundaries is $\omega/N \approx 0.8$ while in the interior $\omega/N \approx 1$, implying close to evanescent waves in the interior, as can be inferred from their almost vertical propagation direction (figure 6c V). The coupling between the top and bottom currents is therefore also weak, and there is amplitude symmetry only for some aspect ratios. In the interior, there is a smooth exchange flow (figure 7a,b V). This regime is referred to as fast corner flow with evanescent internal waves (FCoE).

In case VI, $Pr = 4$, a simulation for a single aspect ratio has been conducted, showing that the oscillation frequency of the instability (here, $\omega/N_c \approx 1.8$) increases further with Pr (see figure 6a–d VI). Internal waves emitted by the buoyancy currents near the top and bottom are evanescent and cannot propagate further into the interior. The two buoyancy currents have again different perturbation amplitudes and are therefore asymmetric in amplitude (figure 6b VI). The scales of motion in the boundary layer, top and bottom buoyancy currents as well as the interior are indeed very different (see figure 6c VI), showing two independent unstable regions. As will be shown below, this is a shear instability located at the wall. This regime is referred to as the fast instability at the wall (FW).

3.2.1. Corner and boundary layer flows

When zooming in the corner regions (figure 8) substantial flow changes can be noticed for different Pr . For $Pr = 0.53$, the detachment and position of L_h (see figure 1b) is small. Rolling vortex billows emerging from shear instability move to the corner (see supplementary movies) leading a maximum of the instability in the boundary layer near

the corner (see [figure 8a,e](#)). For $Pr = 0.71$, the instability has its maxima in the corner in the detached buoyancy current, where the main mixing occurs (see [figure 8b,f](#)). For $Pr = 2.8$, the buoyancy current hardly detaches, and the flow is characterised by the presence of a downward jet close to the wall (at 0.98 in [figure 8c,g](#)). The instability is located inside the detached buoyancy current and close to the boundary ([figure 8g](#)).

For $Pr = 4$, the boundary layer detaches right in the corner region where it also results in a downward return flow ([figure 8d](#)). The temperature gradient has its maximum very near to the wall. Outside the boundary layer, the strong shear between the upward boundary layer motion and the downward return flow with rotary motions similar to that for Kelvin–Helmholtz-type instabilities (see [figure 8d,h](#) and supplementary material) suggests a shear instability (see also Janssen & Henkes 1995; Xu *et al.* 2008). In the interior, there is a horizontal exchange flow from right to left above mid-depth, and below from left to right (see [figure 6](#) with $Pr \geq 0.53$). This exchange flow becomes dominant with increasing Pr .

The phase plots in [figure 6\(c\)](#) V–VI, ($Pr = 2.8$ and $Pr = 4.0$) show a large difference in scale between the boundary layers and the interior. Internal waves in the interior emerge from the buoyancy currents at the top and bottom boundaries, and are related to up- and downward motions of entrainment and detrainment, as shown in [figure 8\(c,d,g,h\)](#). Comparing these latter plots showing the perturbation amplitude ([figure 8g,h](#)), one notices that the downward flow for $Pr = 4.0$ goes to mid-depth, and for $Pr = 2.8$ to only approximately half that distance. In contrast to the case $Pr = 2.8$, for $Pr = 4$ the instability is located at the boundary where it has its maximum amplitude.

3.3. Instabilities and regime diagram

[Figure 9\(a\)](#) presents the normalised oscillation frequency of the leading linear mode with respect to Pr for the four different values of A . Here, N_c varies with Pr (see [figure 5](#)) but the main variation is in ω . The sharp jump at $Pr \approx 0.55 \pm 0.15$ separates two different regimes, one for small Pr and one for large Pr , which can be deduced from scaling arguments (see Gill 1966). From the stationary heat equation, one can deduce that the velocity along the boundary scales as κ/ℓ when ℓ is the length scale of the boundary layer. When introducing this scaling into the vorticity equation, with $\xi = \nabla \times \mathbf{v}_b$, we obtain for the convective term $\mathbf{v}_b \cdot \nabla \xi \sim \kappa^2/\ell^3$ and the diffusive term $v \nabla^2 \xi \sim v\kappa/\ell^3$. The ratio of the diffusive term over the convective term is equal to $Pr = v/\kappa$.

For small Prandtl number the instability is thus convectively driven with large cell circulations (see also [figure 7](#)). In [figure 9\(a\)](#) ($Pr \lesssim 0.5$) the flow is characterised by a cell circulation that is affected by the cavity aspect ratio A . For small cavity widths (large A), the buoyancy current remains attached to the horizontal boundary, and reinforces the motion in the thermal boundary layer at the wall, resulting in a fast motion with a high frequency of oscillation (see e.g. red squares in [figure 5a](#)). For large cavity widths (small A), the buoyancy currents detach from the horizontal boundaries, and radiate internal waves into the interior. The cell circulation is therefore weakened, resulting in a relatively slow motion with a low frequency of oscillation (see e.g. blue squares [figure 5a](#)), and thus a smaller Pr is needed to increase ω/N_c .

For large Prandtl numbers the diffusion term is larger than the convective term, from which it was concluded that the instability is buoyancy driven (see McBain, Armfield & Desrayaud 2007). But the detrainment and entrainment motions and the related return flows that are due to these horizontal boundaries cannot be neglected. Janssen & Henkes (1995) (for different Pr values, 0.25, 0.71 and 2) and Yahata (1999) (for $Pr = 0.71$) suggested this to be a shear instability with a change in instability from shear driven

Vertical convection regimes

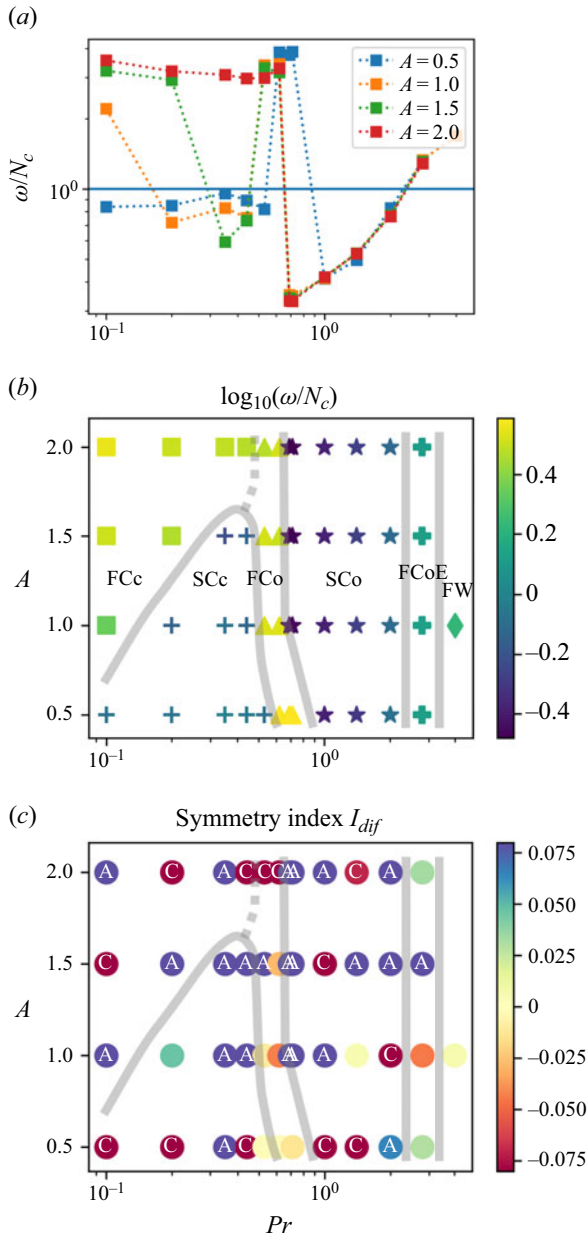


Figure 9. (a) Maximum normalised oscillation frequency (ω/N_c) and (b) regime diagram in space set by Pr and aspect ratio A , with the colour indicating the logarithmic value of the normalised oscillation frequency ω/N_c . Regime names are F for fast when $\omega/N_c > 1$ and S for slow when $\omega/N_c < 1$, ■ fast circulation cells (FCc); + slow circulation cells; ▲ fast corner flow (FCo); ★ slow corner flow (SCo); + fast corner evanescent waves (FCoE), and ◆ fast instability at the wall (FW). (c) Diagram showing the symmetry index I_{dif} (3.7), with the extremes (blue and red) corresponding to symmetric cases (anti-centro-symmetric – letter A – and centro-symmetric – letter C –) and yellow for amplitude asymmetry and no coupling between top and bottom regions.

for $A > 3.65$, to internal wave driven for $A < 3.41$. For the present range in Pr values, [figure 9\(a\)](#) shows strong variations around $Pr = 0.55 \pm 0.15$ before the general trend to thinner boundaries and larger ω/N_c values for $Pr \gtrsim 1$.

The regime diagram in [figure 9\(b\)](#) shows the oscillation frequency ω/N represented by the colour as a function of Pr and aspect ratio A , with the symbols indicating the different regimes discussed above. For $Pr \lesssim 0.5$, the above reasoning with a dominating cell-driven motion is represented in this diagram. But for $Pr > 0.5$, not less than 4 regimes appear due to the changing influences of internal waves (as indicated in [figure 9\(b\)](#) for $Pr > 0.5$) and decreasing thickness of the boundary layer at the wall with Pr . In regime FCo there are no waves and no coupling; in SCo for the majority of cases there are waves and the top and bottom regions couple. For even larger Pr values internal waves weaken, and the thermal boundary layers are thinner (FCoE). For $Pr = 4.0$ (regime FW) there are no waves and no coupling. In contrast to the regime FCo, the instability occurs at the boundary. Since for larger Pr the lateral boundary layers will be even closer to the walls, one may speculate that this regime will not further change. Simulations were tested for aspect ratio, $A = 6$ and $Pr = 0.7$ as in [Xin & Le Quéré \(2006\)](#), showing again the FCc regime. In view of the mentioned increase of the boundary layer thickness with height, and the increasing inertia of the buoyancy current for taller cavities and thus larger L_h , the regime FCo most likely disappears for larger aspect ratio A .

[Figure 9\(c\)](#) shows the amplitude asymmetry according to the definition of (3.7) as a function of Pr and A . In the FCo regime, due to the absence of internal waves and cell circulation, the flow is asymmetric in amplitude. For larger Pr (regime SCo), waves are present, and generally (except for $A = 1$, $Pr = 1.4$) couple the top and bottom regions. Not all flows with internal waves are found to be symmetric in amplitude. Wave patterns in the interior vary considerably depending on the aspect ratio of the cavity and the location of the detachment of the buoyancy currents, and some do not allow for coupling. This may explain the isolated points of asymmetry in amplitude (orange, green and yellow) for regimes with internal waves (SCc, SCo in [figure 9b](#)). In the regime FCoE ($Pr = 2.8$), internal waves are close to evanescent, so that the coupling is generally weak in this regime, causing asymmetry in the amplitude for most cases, and complete asymmetry in the regime FW ($Pr = 4$). Regime FCc is symmetric in amplitude due to the coupling by the cell circulation, and SCc due to internal waves except for one case ($A = 1$ and $Pr = 0.2$). For $Pr \gtrsim 0.5$, the cell circulation was found to increase in strength for larger aspect ratios $A > 1$, and appeared to cause amplitude symmetry also in the regime FCo, thus showing some overlap between the regimes (dashed line in [figure 9b,c](#)). This suggest that, for higher aspect ratios $A \geq 2$ and $Pr < 0.6$, the flow is also dominated by convectively driven cells.

[Figure 9\(c\)](#) also shows anti-centro- and centro-symmetry (letters A and C, respectively). These results are coherent with former results (see e.g. [Burroughs *et al.* 2004](#); [Xin & Le Quéré 2006](#); [Oteski *et al.* 2015](#)). However, no systematic variation with the regime diagram and amplitude asymmetry was found in this context. It is expected that more pertinent results could be found with a continuous parameter variation method (see e.g. [Lyubimova *et al.* 2009](#)). This is left open for further research.

[Figure 9\(a,b\)](#) suggests that there is a transition in instability in the regime $Pr = 0.55 \pm 0.15$. The increase of both the shear and the density gradient between the detached buoyancy currents and the motion in the boundary layer with Pr , make it hard, however, to determine when exactly the instability is buoyancy or shear driven. A quantitative comparison is needed to determine the precise nature of the instability for each Pr . This is undertaken in a separate study.

Vertical convection regimes

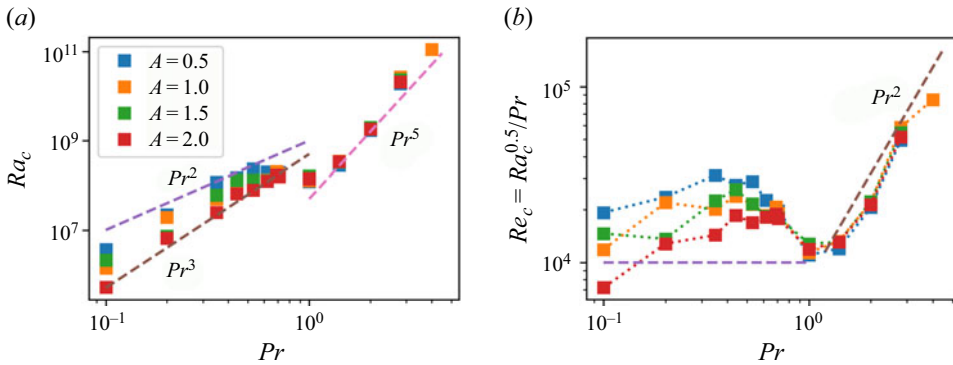


Figure 10. Critical Rayleigh number as a function of Prandtl number and (b) the Reynolds number derived from the critical Rayleigh number and Prandtl number against Prandtl number for different aspect ratios A (see legend). The dashed lines represent the power laws discussed in the text.

Outside the space of this regime diagram, for aspect ratios greater than 3 or 4, the boundary layer will become unstable with, for large Ra , the detachment of vortices disturbing the internal stratification and generating internal waves (Xin & Le Quéré 1995). In the limit of very large Pr and large A , the onset of local cells was found in the core, the number of cells being set by the scale of the instability in the boundary layer (see Daniels 1985, 1987, and references therein).

Figure 10(a,b) shows the variation of the critical Rayleigh number and Reynolds number as a function of Pr , respectively. There is a clear transition between the two regimes, with $Ra_c \sim Pr^2$ for $Pr < 1$ and $Ra_c \sim Pr^5$ for $Pr > 1$. In between (i.e. for $0.5 < Pr \lesssim 2$) there is an intermediate region where internal waves are present and play a role in the dynamics. In both figures 10(a) and 10(b), for $Pr > 1$ the aspect ratio does not affect the results. Finally, it is noteworthy that the Reynolds number defined as $Re_c = Ra_c^{0.5}/Pr$ could serve as an appropriate critical value for the onset of instability since it varies just between $(2 \pm 1)10^4$ for $Pr < 1$, and for $Pr > 1$, $Re_c = 10^4 Pr^2$, whereas the Rayleigh number varies over six decades (see figure 10b). This Reynolds number compares well with a Reynolds number based on the maximum velocity in the cavity and the appropriate typical length scale.

4. Conclusions and discussion

The present investigation shows that there is a large variation in flow regimes depending on the Prandtl number and aspect ratio, as is represented in the regime diagram of figure 9(b). The roles of the detachment in the corner regions and the internal waves in the dynamics are investigated.

The regimes depend on the variation in the detachment of the buoyancy current with Prandtl number and its effect on the circulation inside the cavity, and on the other hand, the presence of internal waves. When there is no detachment (for $Pr < 0.5$) and the buoyancy current is limited by the horizontal extent of the cavity, a cell circulation develops. The instability mode is global, and top and bottom motions have amplitude symmetry, i.e. they have the same (absolute) perturbation amplitude.

When there is detachment of the buoyancy current, there is a local circulation that is determined by the dynamics of the buoyancy current. The coupling between top and bottom motions, and therefore their symmetry in amplitude, then depends on the presence

of internal waves. Generally, in the absence of internal waves and large-scale circulation, the perturbation amplitudes in the corner region differ and the flow is asymmetric. However, some exceptions occur, and not all internal wave patterns allow for this coupling.

The critical Rayleigh number depends on the Prandtl number, with two regimes, one for $Pr < 1$ with some variation due to aspect ratio and $Ra_c \sim Pr^2$, and one for $1 < Pr < 4$ where the aspect ratio does not affect the results and $Ra_c \sim Pr^5$. As mentioned above, this can equally be expressed in terms of the Reynolds number. For our extreme value of $Pr = 4$, Janssen & Henkes (1995) find a critical Rayleigh number $Ra_c = 2.5 \times 10^{10}$, while for $Pr = 10$ Wang *et al.* (2021) find a critical Rayleigh number of $Ra_c = 6 \times 10^{10}$, showing a downward tendency. This subject is open to further research. On the other hand, for very small Prandtl numbers, Gelfgat *et al.* (1999) found critical Ra values of $O(10^{-4})$ so that, on this side, a further decrease in critical Rayleigh number can be expected with higher critical Rayleigh numbers for the smaller aspect ratios A .

Some of the regimes represented in figure 9(b) have been observed in former investigations. For air-filled cavities with aspect ratios of 6 and 7, for example, the FCC regime was also found in Xin & Le Quéré (2006), whereas the SCo regime is well studied in e.g. Le Quéré & Behnia (1998) and Oteski *et al.* (2015), but no detailed information has been found about the instabilities of the FCoE and FW regimes. Most remarkable is the FCo regime with its drastic increase in oscillation frequency of a factor of 10 for Prandtl numbers in the range of $Pr = 0.55 \pm 0.15$. This regime has not been shown before. It most likely disappears for larger aspect ratio, with for $A \leq 2$ and approximately $Pr < 0.55$, the flow being dominated by convectively driven cells.

For $0.4 \leq Pr \leq 0.7$, the shear and the temperature gradient between the corner region and upward motion near the wall increase, and the corner region oscillates with internal waves in the interior. There is uncertainty about the origin of the instability mechanism, and the roles of shear and internal waves. For $Pr > 2.8$ the region of instability changes again and occurs between the downward motion in the detached corner flow and the upward motion at the wall at some distance from the boundary. Also, here, the temperature gradient is large. Therefore, in order to determine the origin of the instability, a comparison of the individual terms in the momentum equations, as well as plots for the Rayleigh criterion, centrifugal instability and Richardson number, is needed. Since this is a rather elaborate effort, it will be presented elsewhere.

This investigation is limited to a single mode, obtained for the lowest critical Ra . When increasing Ra , bifurcations with other modes may appear, as shown by Oteski *et al.* (2015) for $Pr = 0.7$ for air, and in a three-dimensional box by e.g. Gelfgat (2017). In view of former results obtained with direct numerical simulations (see Trias *et al.* 2007), one may nevertheless expect that the present results will provide also a good guideline for the three-dimensional case, as long as the Rayleigh number is small ($Ra < 10^{10}$). Preliminary tests in the present research have shown that three-dimensional instabilities are absent as long as the cavity depth is approximately 10% of the cavity height (i.e. $0.1 \times H$). Therefore, we expect that the present regimes have their footprint also in a quasi-three-dimensional environment.





Supplementary movies. Supplementary movies are available at <https://doi.org/10.1017/jfm.2023.1056>. The data that support the findings of this study are openly available in Zenodo at <https://zenodo.org/records/7827872>, reference number 7827872.

Acknowledgments. The authors thank the anonymous referees for their helpful comments. Further, they acknowledge O. De-Marchi, G. Moreau and C. Bonamy of the LEGI's informatics team for their support.

Funding. This project was funded by the project LEFE/IMAGO-2019 contract COSTRIO. A.K. acknowledges the finance of his PhD thesis from the school STEP of the University Grenoble Alpes. Part of this work was performed using resources provided by CINES under GENCI allocation number A0120107567.

Declaration of interests. The authors report no conflict of interest.

Author ORCIDs.

-  Arman Khoubani <https://orcid.org/0000-0002-0295-5308>;
-  Ashwin Vishnu Mohanan <https://orcid.org/0000-0002-2979-6327>;
-  Pierre Augier <https://orcid.org/0000-0001-9481-4459>;
-  Jan-Bert Flór <https://orcid.org/0000-0002-7114-2263>.

Appendix. Table with input parameters

<i>A</i>	<i>Pr</i>	<i>Ra</i> (10 ⁷)	<i>n_x</i>	<i>n_y</i>	<i>A</i>	<i>Pr</i>	<i>Ra</i> (10 ⁷)	<i>n_x</i>	<i>n_y</i>
0.5	0.1	0.369	80	40	1	0.1	0.1406	40	40
0.5	0.2	2.2	80	40	1	0.2	2.605	40	40
0.5	0.35	12.8	80	40	1	0.35	4.939	40	40
0.5	0.44	16.5	88	44	1	0.44	10.962	44	44
0.5	0.53	24	88	44	1	0.53	14.82	44	44
0.5	0.62	24.1	88	44	1	0.62	13.26	44	44
0.5	0.69	19.85	88	44	1	0.69	20.40	44	44
0.5	0.71	23.75	88	44	1	0.71	18.35	44	44
0.5	1	12.13	96	48	1	1	12.88	48	48
0.5	1.4	28.15	104	52	1	1.4	35.15	52	52
0.5	2	310	160	80	1	2	2000	80	80
0.5	2.8	2880	200	100	1	2.8	2800	100	100
—	—	—	—	—	1	4	11 950	100	100

<i>A</i>	<i>Pr</i>	<i>Ra</i> (10 ⁷)	<i>n_x</i>	<i>n_y</i>	<i>A</i>	<i>Pr</i>	<i>Ra</i> (10 ⁷)	<i>n_x</i>	<i>n_y</i>
1.5	0.1	0.213	27	40	2	0.1	0.594200	20	40
1.5	0.2	0.739	27	40	2	0.2	0.6408	20	40
1.5	0.35	6.19	27	40	2	0.35	2.6788	20	40
1.5	0.44	13.2	33	50	2	0.44	6.7	28	56
1.5	0.53	13.18	33	50	2	0.53	7.95	25	50
1.5	0.62	12.135	33	50	2	0.62	12.63	25	50
1.5	0.69	18.26	33	50	2	0.69	17	25	50
1.5	0.71	16.325	33	50	2	0.71	15.87	25	50
1.5	1	158	37	56	2	1	14.125	28	56
1.5	1.4	34.1	40	60	2	1.4	34.15	30	60
1.5	2	197.2	53	80	2	2	181.25	40	80
1.5	2.8	2600	80	120	2	2.8	2500	60	120

Table 1. Input parameters for the linear simulations. Here, *n_x* and *n_y* are the number of elements in the *x* and *y* directions, respectively, and the polynomial order *O* is for all cases 7 so that the number of grid points is (*O* + 1)² × *n_x* × *n_y*.

REFERENCES

- ÅKERVIK, E., BRANDT, L., HENNINGSON, D.S., HØPEFFNER, J., MARXEN, O. & SCHLATTER, P. 2006 Steady solutions of the Navier–Stokes equations by selective frequency damping. *Phys. Fluids* **18** (6), 068102.
- AUGIER, P., MOHANAN, A.V. & BONAMY, C. 2019 FluidDyn: a python open-source framework for research and teaching in fluid dynamics by simulations, experiments and data processing. *J. Open Res. Softw.* **7**, 9.
- BEJAN, A. 2013 *Convection Heat Transfer*. John Wiley & Sons.
- BENGANA, Y., LOISEAU, J.-C., ROBINET, J.-C. & TUCKERMAN, L.S. 2019 Bifurcation analysis and frequency prediction in shear-driven cavity flow. *J. Fluid Mech.* **875**, 725–757.
- BURROUGHS, E.A., ROMERO, L.A., LEHOUCQ, R.B. & SALINGER, A.G. 2004 Linear stability of flow in a differentially heated cavity via large-scale eigenvalue calculations. *Intl J. Numer. Meth. Heat Fluid Flow* **14** (6), 803–822.
- BUSSE, F.H. 2006 Bénard convection and geophysical applications. In *Dynamics of Spatio-Temporal Cellular Structures: Henri Bénard Centenary Review* (ed. I. Mutabazi, J.E. Wesfreid & E. Guyon), pp. 103–125. Springer.
- CHENOWETH, D.R. & PAOLUCCI, S. 1986 Natural convection in an enclosed vertical air layer with large horizontal temperature differences. *J. Fluid Mech.* **169**, 173–210.
- DANIELS, P.G. 1985 Stationary instability of the buoyancy-layer flow between heated vertical planes. *Proc. R. Soc. Lond. A* **401** (1820), 145–161.
- DANIELS, P.G. 1987 Convection in a vertical slot. *J. Fluid Mech.* **176**, 419–441.
- GARAUD, P. 2021 Journey to the center of stars: the realm of low Prandtl number fluid dynamics. *Phys. Rev. Fluids* **6**, 030501.
- GELFGAT, A.Y. 2017 Time-dependent modeling of oscillatory instability of three-dimensional natural convection of air in a laterally heated cubic box. *Theor. Comput. Fluid Dyn.* **31** (4), 447–469.
- GELFGAT, A.Y. 2020a Instability of natural convection in a laterally heated cube with perfectly conducting horizontal boundaries. *Theor. Comput. Fluid Dyn.* **34** (5–6), 693–711.
- GELFGAT, A.Y. 2020b Instability of natural convection of air in a laterally heated cube with perfectly insulated horizontal boundaries and perfectly conducting spanwise boundaries. *Phys. Rev. Fluids* **5** (9), 093901.
- GELFGAT, A.Y., BAR-YOSPEH, P.Z. & YARIN, A.L. 1999 Stability of multiple steady states of convection in laterally heated cavities. *J. Fluid Mech.* **388**, 315–334.
- GILL, A.E. 1966 The boundary-layer regime for convection in a rectangular cavity. *J. Fluid Mech.* **26** (3), 515–536.
- GRAYER, H., YALIM, J., WELFERT, B.D. & LOPEZ, J.M. 2020 Dynamics in a stably stratified tilted square cavity. *J. Fluid Mech.* **883**.
- GRÖTZBACH, G. 2013 Challenges in low-Prandtl number heat transfer simulation and modelling. *Nucl. Engng Des.* **264**, 41–55.
- GUERVILLY, C., CARDIN, P. & SCHAEFFER, N. 2019 Turbulent convective length scale in planetary cores. *Nature* **570** (7761), 368–371.
- VAN HEIJST, G.J.F., CLERCX, H.J.H. & MOLENAAR, D. 2006 The effects of solid boundaries on confined two-dimensional turbulence. *J. Fluid Mech.* **554** (–1), 411–431.
- HENKES, R.A.W.M. & HOOGENDOORN, C.J. 1990 On the stability of the natural convection flow in a square cavity heated from the side. *Appl. Sci. Res.* **47** (3), 195–220.
- JANSSEN, R.J.A. & HENKES, R.A.W.M. 1995 Influence of Prandtl number on instability mechanisms and transition in a differentially heated square cavity. *J. Fluid Mech.* **290**, 319–344.
- VAN DE KONIJNENBERG, J.A., FLOR, J.B. & VAN HEIJST, G.J.F. 1998 Decaying quasi-two-dimensional viscous flow on a square domain. *Phys. Fluids* **10** (3), 595–606.
- LAPPA, M. 2009 *Thermal Convection: Patterns, Evolution and Stability*. John Wiley & Sons.
- LE QUÉRÉ, P. 2022 Natural convection in air-filled differentially heated isoflux cavities: scalings and transition to unsteadiness, a long story made short. *Intl J. Therm. Sci.* **176**, 107430.
- LE QUÉRÉ, P. & BEHNIA, M. 1998 From onset of unsteadiness to chaos in a differentially heated square cavity. *J. Fluid Mech.* **359** (1), 81–107.
- LYUBIMOVA, T.P., LYUBIMOV, D.V., MOROZOV, V.A., SCURIDIN, R.V., HADID, H.B. & HENRY, D. 2009 Stability of convection in a horizontal channel subjected to a longitudinal temperature gradient. Part 1. Effect of aspect ratio and Prandtl number. *J. Fluid Mech.* **635**, 275–295.
- MCBAIN, G.D., ARMFIELD, S.W. & DESRAYAUD, G. 2007 Instability of the buoyancy layer on an evenly heated vertical wall. *J. Fluid Mech.* **587**, C92–17.
- MIROSHNICHENKO, I.V. & SHEREMET, M.A. 2018 Turbulent natural convection heat transfer in rectangular enclosures using experimental and numerical approaches: a review. *Renew. Sustain. Energy Rev.* **82** (Part 1), 40–59.

Vertical convection regimes

- MOHANAN, A.V., BONAMY, C., LINARES, M.C. & AUGIER, P. 2019 FluidSim: modular, object-oriented Python package for high-performance CFD simulations. *J. Open Res. Softw.* **7**, 14.
- MOHANAN, A.V., KHOUBANI, A. & AUGIER, P. 2023 SneK5000: a new Python framework for Nek5000. *J. Open Source Softw.* **8** (88), 5586.
- OTESKI, L., DUGUET, Y., PASTUR, L. & LE QUÉRÉ, P. 2015 Quasiperiodic routes to chaos in confined two-dimensional differential convection. *Phys. Rev. E* **92** (4), 043020.
- PANDEY, A., SCHUMACHER, J. & SREENIVASAN, K.R. 2021 Non-Boussinesq low-Prandtl-number convection with a temperature-dependent thermal diffusivity. *Astrophys. J.* **907** (1), 56.
- PAOLUCCI, S. 1990 Direct numerical simulation of two-dimensional turbulent natural convection in an enclosed cavity. *J. Fluid Mech.* **215**, 229–262.
- PAOLUCCI, S. & CHENOWETH, D.R. 1989 Transition to chaos in a differentially heated vertical cavity. *J. Fluid Mech.* **201**, 379–410.
- TRIAS, F.X., SORIA, M., OLIVA, A. & PÉREZ-SEGARRA, C.D. 2007 Direct numerical simulations of two- and three-dimensional turbulent natural convection flows in a differentially heated cavity of aspect ratio 4. *J. Fluid Mech.* **586**, 259–235.
- WANG, Q., LIU, H.-R., VERZICCO, R., SHISHKINA, O. & LOHSE, D. 2021 Regime transitions in thermally driven high-Rayleigh number vertical convection. *J. Fluid Mech.* **917**, A6.
- WU, K., WELFERT, B.D. & LOPEZ, J.M. 2018 Complex dynamics in a stratified lid-driven square cavity flow. *J. Fluid Mech.* **855**, 43–66.
- XIN, S. & LE QUÉRÉ, P. 2012 Stability of two-dimensional (2D) natural convection flows in air-filled differentially heated cavities: 2D/3D disturbances. *Fluid Dyn. Res.* **44** (3), 031419.
- XIN, S. & LE QUÉRÉ, P. 1995 Direct numerical simulations of two-dimensional chaotic natural convection in a differentially heated cavity of aspect ratio 4. *J. Fluid Mech.* **304**, 87–118.
- XIN, S. & LE QUÉRÉ, P. 2006 Natural-convection flows in air-filled, differentially heated cavities with adiabatic horizontal walls. *Numer. Heat Transfer A* **50** (5), 437–466.
- XU, F., PATTERSON, J.C. & LEI, C. 2008 On the double-layer structure of the boundary layer adjacent to a sidewall of a differentially heated cavity. *Intl J. Heat Mass Transfer* **51** (15–16), 3803–3815.
- YAHATA, H. 1999 Stability analysis of natural convection in vertical cavities with lateral heating. *J. Phys. Soc. Japan* **68** (2), 446–460.